AAS 25-767

SUNDMAN-TRANSFORMED CONVEX LOW-THRUST TRAJECTORY OPTIMIZATION IN MULTI-BODY SYSTEMS

Christian Hofmann[*], Kai Xi[†], Hakan Chunton[‡], Giovanni Lavezzi[§], Ethan R. Burnett[¶], Francesco Topputo[‖] and Richard Linares[**]

With numerous near-future missions planned to the Moon, rapid and reliable trajectory design in complex multi-body models is essential. In this work, we improve the sequential convex programming (SCP) approach in multi-body systems by addressing the convergence issues in highly nonlinear regions using a Sundman transformation in the rotating-pulsating frame. Moreover, we extend previous work to solve continuous thrust problems. The efficacy of the proposed approach is shown in orbital transfers in the Sun-Earth-Moon system.

INTRODUCTION

Interest in lunar and deep space missions has grown significantly in recent years. NASA's Artemis program plans to establish a long-term presence in lunar and cislunar space, while commercial efforts from Blue Origin and Intuitive Machines focus on creating reliable and economically sustainable lunar access. Trajectory design for unmanned missions generally prioritizes fuel efficiency and operational constraints, but crewed missions must also account for factors like time-of-flight and abort options. These requirements are challenging to balance due to the complex gravitational interactions involved. To address this, mission designers increasingly rely on multi-body dynamics, which allow for more efficient trajectories than traditional two-body models. Even simplified approximations using two or three gravitational bodies can offer meaningful insights into the system's structure. The circular restricted three-body problem (CRTBP) is the most commonly used model for lunar and cislunar transfers thanks to its simplicity [1], but its low fidelity can limit its accuracy. As a result, more advanced models such as the elliptic restricted three-body problem (ERTBP) and the bi-circular restricted four-body problem (BCRFBP) have been proposed to improve realism [2].

[*]Postdoctoral Associate, Department of Aeronautics and Astronautics, Massachusetts Institute of Technology, Cambridge, MA 02139, USA, *hofmannc@mit.edu.*

[†]Undergraduate Student, Department of Aeronautics and Astronautics, Massachusetts Institute of Technology, MA 02139, USA, *xkai@mit.edu.*

[‡]Undergraduate Student, Department of Aeronautics and Astronautics, Massachusetts Institute of Technology, MA 02139, USA, *hchunton@mit.edu.*

[§]Postdoctoral Associate, Department of Aeronautics and Astronautics, Massachusetts Institute of Technology, Cambridge, MA 02139, USA, *glavezzi@mit.edu.*

[¶]Marie Skłodowska-Curie Postdoctoral Fellow, Department of Aerospace Science and Technology, Politecnico di Milano, 20159 Milan, Italy, *ethanryan.burnett@polimit.it*

[‖]Full Professor, Department of Aerospace Science and Technology, Politecnico di Milano, 20159 Milan, Italy, *francesco.topputo@polimi.it*

[**]Associate Professor, Department of Aeronautics and Astronautics, Massachusetts Institute of Technology, Cambridge, MA 02139, USA, *linaresr@mit.edu*

Several prior studies have explored the transition between lower- and higher-fidelity models in the context of single rotating-pulsating systems. Park et al. investigated the intermediate models seen in these works using a dynamical systems theory perspective [3]. Sanaga et al. directly developed a transition scheme for trajectories in a low-fidelity model using a multiple-shooting scheme to gradually shift the dynamics [4]. Xi et al. developed a homotopic scheme for optimizing impulsive trajectories in higher-fidelity models by gradually increasing the fidelity of the dynamics in a similar way using a sequential convex programming (SCP) framework [5]. However, this approach often fails to converge due to the highly nonlinear dynamics in multi-body transfers. In the present work, we improve upon the SCP framework used for optimizing trajectories in higher-fidelity models and address the limitations of previous works. We extend prior efforts by: (1) applying a Sundman transformation across the CRTBP, BCRFBP, and rotating-pulsating n-body problem (RPNBP) dynamics to improve convergence near highly nonlinear regions such as planets; and (2) incorporating low-thrust acceleration into the Sundman-transformed equations of motion to enable flexible, lower-propellant trajectory design.

The paper is structured as follows. The dynamical models and problem formulation are described first, and then the Sundman transformation is introduced. Subsequently, the simulation and results are presented. Finally, concluding remarks are provided.

DYNAMICAL MODELS AND PROBLEM FORMULATION

Dynamical Models

We use the equations of motion written in the rotating-pulsating frame (see Fig. 1) [6]:

$$\boldsymbol{\rho}'' = \underbrace{\begin{bmatrix} m_1 \\ m_2 \\ m_3 \end{bmatrix}}_{=:\mathbf{m}_1} + \underbrace{\begin{bmatrix} m_4 & m_5 & 0 \\ -m_5 & m_4 & m_6 \\ 0 & -m_6 & m_4 \end{bmatrix}}_{=:\mathbf{M}_2} \boldsymbol{\rho}' + \underbrace{\begin{bmatrix} m_7 & m_9 & m_8 \\ -m_9 & m_{10} & m_{11} \\ m_8 & -m_{11} & m_{12} \end{bmatrix}}_{=:\mathbf{M}_3} \boldsymbol{\rho} + m_{13} \nabla \Omega \tag{1}$$

where $(\cdot)'$ denotes the derivative with respect to the nondimensional time τ, and

$$\Omega = \frac{\mu_{P_1}}{\|\boldsymbol{\rho} - \boldsymbol{\rho}_{P_1}\|} + \frac{\mu_{P_2}}{\|\boldsymbol{\rho} - \boldsymbol{\rho}_{P_1}\|} + \sum_{j \in \mathcal{A}} \frac{\mu_j}{\|\boldsymbol{\rho} - \boldsymbol{\rho}_j\|} \tag{2}$$

The points P_1, P_2, s/c, and A_j in Fig. 1 refer to the two primaries, the spacecraft, and other perturbing bodies in the set $\mathcal{A}$, respectively. μ_{P_1}, μ_{P_2}, and μ_j denote the corresponding nondimensional gravitational parameters, and $\boldsymbol{\rho}_{P_1}$, $\boldsymbol{\rho}_{P_2}$, and $\boldsymbol{\rho}_j$ refer to the (nondimensional) positions in the rotating-pulsating frame. B denotes the origin and the center of mass between P_1 and P_2. Note that all quantities are nondimensional. Even though the distance between the primaries ℓ varies over time, one characteristic of the pulsating frame is that this distance is always kept at unit length.

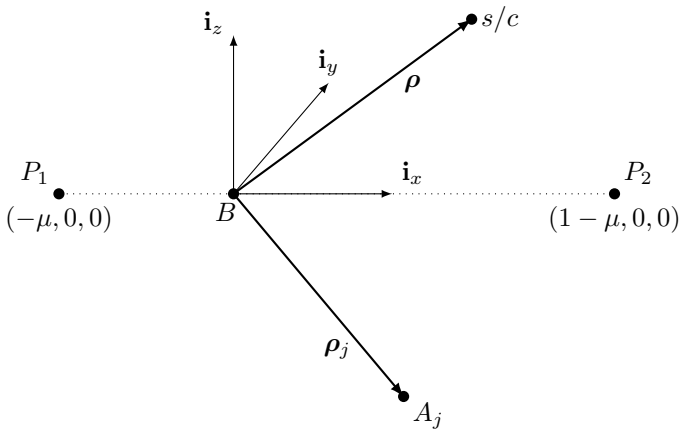

Figure 1: Pulsating-rotating frame.

The coefficients m_1 to m_{13} are given by [5]

$$\mathbf{m}_1 = -\frac{1}{\ell\,\dot{\tau}^2}\,\mathbf{C}^\top \ddot{\mathbf{b}} \tag{3}$$

$$\mathbf{M}_2 = -\frac{\ell}{\dot{\tau}}\left[\left(\frac{2\,\dot{\ell}}{\ell} + \frac{\ddot{\tau}}{\dot{\tau}}\right)\mathbf{I}_3 + 2\,\mathbf{C}^\top \dot{\mathbf{C}}\right] \tag{4}$$

$$\mathbf{M}_3 = -\frac{1}{\dot{\tau}^2}\left[\frac{\ddot{\ell}}{\ell}\,\mathbf{I}_3 + \frac{2\,\dot{\ell}}{\ell}\,\mathbf{C}^\top \dot{\mathbf{C}} + \mathbf{C}^\top \ddot{\mathbf{C}}\right] \tag{5}$$

$$m_{13} = \frac{\tilde{\mu}_{P_1} + \tilde{\mu}_{P_2}}{\ell^3\,(\dot{\tau})^2} \tag{6}$$

where $\mathbf{b}$ is the vector from the origin to the barycenter B in the inertial frame, $\mathbf{C}$ is a rotation matrix, $\mathbf{I}_{3\times 3}$ the 3×3 identity matrix, and $\tilde{\mu}_{P_1}$ and $\tilde{\mu}_{P_2}$ denote the dimensional gravitational parameters of the two primaries. $\dot{(\cdot)}$ refers to the derivative with respect to the physical time t. Relevant quantities and derivatives are given in [5, 6, 7]. We also assume a nonuniform flow of time where the instantaneous distance between the two primaries is used for scaling, and the characteristic time t_c is given by

$$t_c = \sqrt{\frac{\tilde{\mu}_{P_1} + \tilde{\mu}_{P_2}}{\ell^3}} \tag{7}$$

Problem Formulation

We formulate the trajectory optimization problem for two distinct types of propulsion: impulsive maneuvers and continuous low thrust. The core of our approach involves solving a sequence of convexified problems.

First, we consider the impulsive thrust case. The trajectory is optimized by solving the following convex problem:

$$\underset{\mathbf{u}_i}{\text{minimize}} \quad \sum_{i=1}^{n_\mathrm{u}} \|\mathbf{u}_i\|^2 + \lambda_\nu \|\boldsymbol{\nu}\|_1 \tag{8a}$$

$$
\begin{aligned}
\text{subject to:} \quad & \dot{\mathbf{x}} = \mathbf{f}(\mathbf{x}, \mathbf{u}_i) + \boldsymbol{\nu} && \text{(8b)}\\
& \|\mathbf{u}_i\| \leq \Delta v_{\max} && \text{(8c)}\\
& \|\mathbf{x} - \bar{\mathbf{x}}\|_1 \leq R && \text{(8d)}\\
& \mathbf{x}(t_0) = \mathbf{x}_0 && \text{(8e)}\\
& \mathbf{x}(t_f) = \mathbf{x}_f && \text{(8f)}
\end{aligned}
$$

In this formulation, the state vector is $\mathbf{x} = [\mathbf{r}, \mathbf{v}]^\top$, representing the spacecraft's position and velocity. The controls $\mathbf{u}_i$ are the n_u impulsive maneuvers. The objective function (8a) seeks to minimize the total squared control effort. To enhance convergence and prevent artificial infeasibility during the SCP process, unconstrained virtual controls $\boldsymbol{\nu}$ are added to the dynamics and penalized in the cost function by a positive scaling factor λ_ν [8].

The dynamics in Eq. (8b) are linearized around the solution from the previous iteration, $\bar{\mathbf{x}}$. The constraints include a maximum magnitude $\Delta v_{\max}$ for each maneuver (8c), a trust-region radius R to confine the solution to the neighborhood of the reference trajectory (8d), and prescribed initial and final boundary conditions, $\mathbf{x}_0$ and $\mathbf{x}_f$ (8e)-(8f).

Maneuvers are permitted at the N discretization nodes. The linearized and discretized dynamics between nodes are given by:

$$
\mathbf{f}(\mathbf{x}_k, \mathbf{u}_k) = \begin{cases} \mathbf{A}_k\,\mathbf{x}_k + \mathbf{B}_k\,\mathbf{u}_k + \mathbf{q}_k, & \text{if } \mathbf{u}_k \neq \mathbf{0} \text{ at } t_k \\ \mathbf{A}_k\,\mathbf{x}_k + \mathbf{q}_k, & \text{otherwise} \end{cases} \tag{9}
$$

where $(\cdot)_k \coloneqq (\cdot)(t_k)$ for $k = 0, \ldots, N-1$. If an impulsive maneuver occurs at time t_k, its effect is modeled by the matrix $\mathbf{B}_k \equiv [\mathbf{0}_3, \mathbf{I}_3]^\top$, where $\mathbf{0}_3$ and $\mathbf{I}_3$ are the 3×3 zero and identity matrices, respectively. The discrete-time matrices $\mathbf{A}_k$ and $\mathbf{q}_k$ are computed as:

$$
\begin{aligned}
\mathbf{A}_k &= \boldsymbol{\Phi}(t_{k+1}, t_k) && \text{(10a)}\\
\mathbf{q}_k &= \mathbf{A}_k \int_{t_k}^{t_{k+1}} \boldsymbol{\Phi}^{-1}(t, t_k)\,\mathbf{q}(t)\,\mathrm{d}t && \text{(10b)}
\end{aligned}
$$

where $\boldsymbol{\Phi}(\cdot,\cdot)$ is the state transition matrix. The vector $\mathbf{q}(t) = \mathbf{f}(\bar{\mathbf{x}}, t) - \mathbf{f}_\mathbf{x}\,\bar{\mathbf{x}}$ represents the constant part of the linearization of the dynamics $\mathbf{f} = [\boldsymbol{\rho}', \boldsymbol{\rho}'']^\top$ around the reference state $\bar{\mathbf{x}}$. The Jacobian matrix $\mathbf{f}_\mathbf{x}$ is given by:

$$
\mathbf{f}_\mathbf{x} = \begin{bmatrix} \mathbf{0}_3 & \mathbf{I}_3 \\ \mathbf{M}_3 + m_{13}\,\frac{\partial}{\partial \boldsymbol{\rho}}\nabla\Omega & \mathbf{M}_2 \end{bmatrix} \tag{11}
$$

where the gradient of the potential is:

$$
\frac{\partial}{\partial \boldsymbol{\rho}}\nabla\Omega = \sum_{j \in \mathcal{S}} \mu_j \left[-\frac{\mathbf{I}_3}{\|\boldsymbol{\rho} - \boldsymbol{\rho}_j\|^3} + \frac{3\,(\boldsymbol{\rho} - \boldsymbol{\rho}_j)\,(\boldsymbol{\rho} - \boldsymbol{\rho}_j)^\top}{\|\boldsymbol{\rho} - \boldsymbol{\rho}_j\|^5} \right] \tag{12}
$$

The set $\mathcal{S}$ includes all primaries and perturbing bodies. Both $\mathbf{A}_k$ and $\mathbf{q}_k$ are computed by simultaneously integrating the state transition matrix and the nonlinear dynamics from t_k to t_{k+1}.

For the continuous low-thrust case, the problem is formulated as an optimal control problem. The dynamics include a continuous control acceleration $\mathbf{T}/m$, where $\mathbf{T}$ is the thrust vector and m is the spacecraft mass. To simplify the formulation, we introduce several variable changes. First,

to reduce nonlinearities, we define a new state $\omega \coloneqq \ln m$ to track the mass evolution. Second, the nonconvex control term $\mathbf{T}/m$ is replaced by a new control vector $\mathbf{u} \coloneqq \mathbf{T}/m$, which appears linearly in the dynamics. Finally, we introduce an additional control variable $\Gamma \coloneqq \|\mathbf{u}\|_2$.

The resulting low-thrust trajectory optimization problem is:

$$\begin{aligned}
\underset{\mathbf{u},\Gamma}{\text{minimize}} \quad & -\omega(t_f) + \lambda_\nu \|\boldsymbol{\nu}\|_1 + \lambda_\eta \max(0,\eta) && \text{(13a)}\\
\text{subject to:} \quad & \dot{\mathbf{x}} = \mathbf{f}(\mathbf{x},\mathbf{u},\Gamma) + \boldsymbol{\nu} && \text{(13b)}\\
& \Gamma \le T_{\max}\, \mathrm{e}^{-\bar{\omega}} (1 - \omega + \bar{\omega}) + \eta && \text{(13c)}\\
& \|\mathbf{u}\| \le \Gamma && \text{(13d)}\\
& \|\mathbf{x} - \bar{\mathbf{x}}\|_1 \le R && \text{(13e)}\\
& \mathbf{x}(t_0) = \mathbf{x}_0 && \text{(13f)}\\
& \mathbf{x}(t_f) = \mathbf{x}_f && \text{(13g)}
\end{aligned}$$

Here, the objective is to maximize the final mass, which is equivalent to minimizing $-\omega(t_f)$. Equation (13c) is the linearized constraint on the maximum thrust magnitude $T_{\max}$. The slack variable $\eta \ge 0$, penalized by $\lambda_\eta > 0$, is included to avoid artificial infeasibility. Equation (13d) serves as a lossless convex relaxation of the nonconvex constraint $\|\mathbf{u}\|_2 = \Gamma$.

The differential equation for the mass state ω is:

$$\dot{\omega} = -\frac{\Gamma}{g_0\, I_{\mathrm{sp}}} \tag{14}$$

where g_0 is the standard gravitational acceleration and I_{sp} is the specific impulse.

For discretization, we use a first-order-hold (FOH) method on the combined control vector $\tilde{\mathbf{u}} \coloneqq [\mathbf{u}, \Gamma]^\top$. The discretized dynamics are then expressed as:

$$\mathbf{f}(\mathbf{x}_k, \tilde{\mathbf{u}}_k) = \mathbf{A}_k\, \mathbf{x}_k + \mathbf{B}_k^-\, \tilde{\mathbf{u}}_k + \mathbf{B}_k^+\, \tilde{\mathbf{u}}_{k+1} + \mathbf{q}_k \tag{15}$$

The matrices $\mathbf{B}_k^-$ and $\mathbf{B}_k^+$ correspond to the influence of the controls at the start and end of the time interval $[t_k, t_{k+1}]$, respectively:

$$\mathbf{B}_k^- = \mathbf{A}_k \int_{t_k}^{t_{k+1}} \boldsymbol{\Phi}^{-1}(t, t_k)\, \mathbf{B}(t)\, \lambda_-(t)\, \mathrm{d}t \tag{16a}$$

$$\mathbf{B}_k^+ = \mathbf{A}_k \int_{t_k}^{t_{k+1}} \boldsymbol{\Phi}^{-1}(t, t_k)\, \mathbf{B}(t)\, \lambda_+(t)\, \mathrm{d}t \tag{16b}$$

In these expressions, $\mathbf{B}(t)$ is the Jacobian matrix with respect to the control vector $\tilde{\mathbf{u}}$, while $\lambda_-(t)$ and $\lambda_+(t)$ are the linear interpolation factors for the FOH:

$$\lambda_-(t) = \frac{t_{k+1} - t}{t_{k+1} - t_k}, \qquad \lambda_+(t) = \frac{t - t_k}{t_{k+1} - t_k}, \qquad t \in [t_k, t_{k+1}] \tag{17}$$

SUNDMAN TRANSFORMATION

The generalized Sundman transformation is a powerful technique in astrodynamics, traditionally used to improve the computational efficiency of propagating highly elliptical orbits in two-body

problems [9]. By changing the independent variable from time to an angle-like quantity, the transformation allows for a more rapid and stable integration without sacrificing accuracy. It has also been applied to trajectory optimization to solve many-revolution problems using differential dynamic programming [10] and to develop adaptive mesh refinement schemes where node density is increased near the central body [11]. In this work, we adapt and extend this transformation to the CRTBP and higher-fidelity multi-body models, specifically for use within a SCP framework in the rotating-pulsating frame.

For a two-body system, the classical generalized Sundman transformation relates the physical time t to a new independent variable s through the expression:

$$\mathrm{d}t = c\, r^n \, \mathrm{d}s \tag{18}$$

where r is the distance to the central body, n is a chosen exponent, and c is a constant, often selected such that s corresponds to the eccentric or true anomaly. For our application to multi-body dynamics, we define a modified Sundman transformation as:

$$\mathrm{d}\tau = s_0\, c\, r^n \, \mathrm{d}s \tag{19}$$

Here, τ is the nondimensional time, s_0 is an additional normalization factor, and r can represent the distance to either the first or second primary body. The constant c is non-dimensionalized using the characteristic length ℓ and time t_c:

$$c = \frac{t_c}{\ell^n} \tag{20}$$

Using Eq. (19), the first and second derivatives with respect to nondimensional time τ can be re-expressed in terms of the new independent variable s:

$$\frac{\mathrm{d}}{\mathrm{d}\tau} = \frac{1}{s_0\, c\, r^n} \frac{\mathrm{d}}{\mathrm{d}s} \tag{21}$$

$$\frac{\mathrm{d}^2}{\mathrm{d}\tau^2} = -\frac{n}{s_0^2\, c^2\, r^{2n+1}} \frac{\mathrm{d}r}{\mathrm{d}s} \frac{\mathrm{d}}{\mathrm{d}s} + \frac{1}{s_0^2\, c^2\, r^{2n}} \frac{\mathrm{d}^2}{\mathrm{d}s^2} \tag{22}$$

Substituting these into the original equations of motion in Eq. (1), we obtain the transformed dynamics in the s-domain:

$$\boldsymbol{\rho}'' = s_0^2\, c^2\, r^{2n} \, (\mathbf{m}_1 + \mathbf{M}_3\, \boldsymbol{\rho} + m_{13}\, \nabla\Omega) + \left(s_0\, c\, r^n\, \mathbf{M}_2 + \frac{n\, r'}{r}\, \mathbf{I}_3 \right) \boldsymbol{\rho}' \tag{23}$$

where $(\cdot)'$ denotes the derivative with respect to s.

Since many optimization problems include a fixed final time constraint, we augment the state by including the nondimensional physical time τ. Its evolution is governed by:

$$\frac{\mathrm{d}\tau}{\mathrm{d}s} = \tau' = s_0\, c\, r^n \tag{24}$$

For an impulsive trajectory, the state dynamics vector $\mathbf{f}$ can be written as:

$$\mathbf{f} = \begin{bmatrix} \boldsymbol{\rho}' \\ \boldsymbol{\rho}'' \\ \tau' \end{bmatrix} \tag{25}$$

The corresponding Jacobian matrix $\mathbf{f_x}$ for the state vector $\mathbf{x} = [\boldsymbol{\rho}, \boldsymbol{\rho}', \tau]^\top$ is then:

$$\mathbf{f_x} = \frac{\partial \mathbf{f}}{\partial \mathbf{x}} = \begin{bmatrix} \frac{\partial \boldsymbol{\rho}'}{\partial \boldsymbol{\rho}} & \frac{\partial \boldsymbol{\rho}'}{\partial \boldsymbol{\rho}'} & \frac{\partial \boldsymbol{\rho}'}{\partial \tau} \\ \frac{\partial \boldsymbol{\rho}''}{\partial \boldsymbol{\rho}} & \frac{\partial \boldsymbol{\rho}''}{\partial \boldsymbol{\rho}'} & \frac{\partial \boldsymbol{\rho}''}{\partial \tau} \\ \frac{\partial \tau'}{\partial \boldsymbol{\rho}} & \frac{\partial \tau'}{\partial \boldsymbol{\rho}'} & \frac{\partial \tau'}{\partial \tau} \end{bmatrix} \tag{26}$$

The partial derivatives are detailed in the appendix.

While defining r as the distance to a single primary is often sufficient, trajectories involving close passes of both primaries require a more sophisticated approach. For such cases, we propose a weighted effective distance r_{eff} that ensures a smooth transition between the distance to the first primary, r_p, and the second primary, r_s:

$$r_{\text{eff}}^n \coloneqq w\, r_p^n + (1 - w)\, r_s^n \tag{27}$$

The transition is controlled by the weight w:

$$w = \frac{1}{1 + \left(\frac{r_p}{r_s}\right)^k} \tag{28}$$

where the exponent $k > 0$ determines the sharpness of the transition. When the spacecraft is much closer to the first primary ($r_p \ll r_s$), the ratio $r_p/r_s \ll 1$, causing $w \to 1$ and thus $r_{\text{eff}}^n \to r_p^n$. Conversely, when the spacecraft is near the second primary ($r_s \ll r_p$), the ratio $r_p/r_s \gg 1$, causing $w \to 0$ and $r_{\text{eff}}^n \to r_s^n$. This formulation automatically increases the density of discretization nodes in regions near either primary. As both r_{eff}^n and w are smooth and differentiable, their derivatives are readily computed, as shown in Appendix A.

The key advantage of this transformation within an SCP context is its ability to "slow down" the dynamics in the s-domain when the spacecraft is near a primary body. This effectively places more discretization nodes in these highly nonlinear gravitational regions, which significantly aids the convergence of the optimization algorithm. We found that a naive approach of simply adding more nodes manually in the physical time domain failed to produce convergence in our test cases.

Figure 2 illustrates this effect for an orbit in the Earth-Moon CRTBP, where the red segments indicate regions of higher node density resulting from proximity to a primary. This "slowing down" of the dynamics is also evident in Figure 3a, which shows the evolution of physical time τ with respect to s. The flat portions of the curve correspond directly to the dense-node regions. Figure 3b provides a clear visualization of this increased node density.

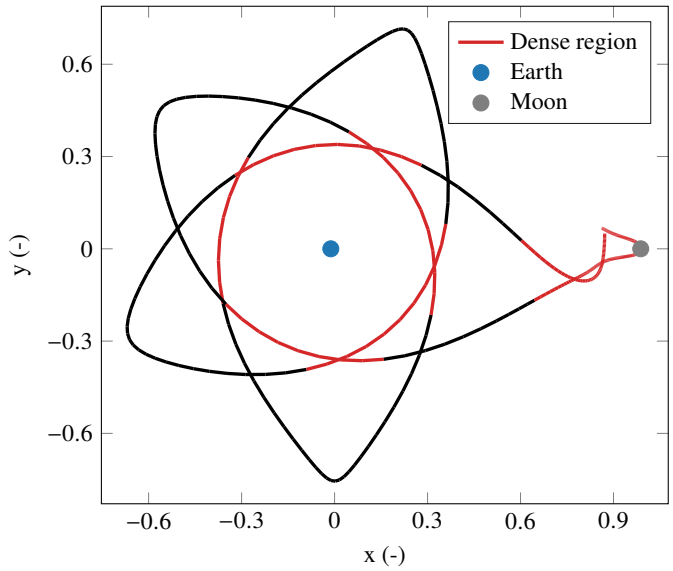

Figure 2: Example trajectory illustrating node clustering under the Sundman transformation.

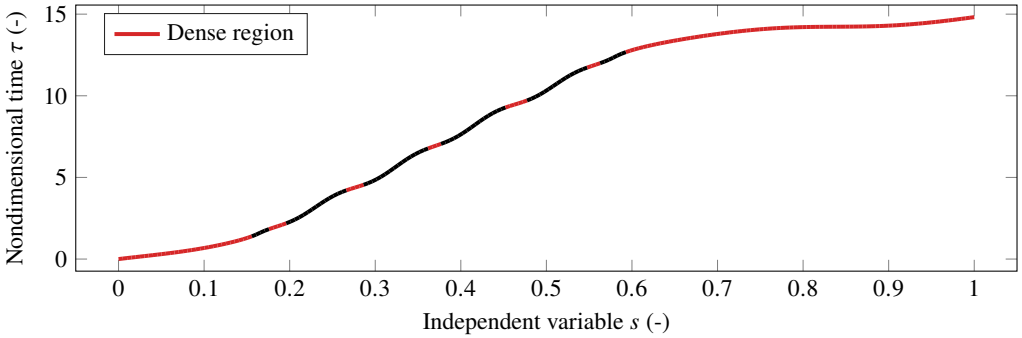

(a) Evolution of nondimensional time.

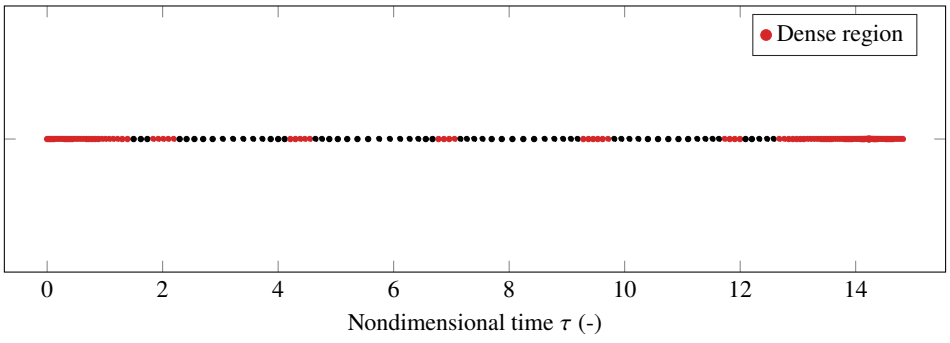

(b) Node distribution.

Figure 3: Evolution of nondimensional time and node distribution.

Sundman-Transformed SCP

A direct consequence of changing the independent variable from τ to s is that an initially fixed-time problem becomes a free-time problem, because the final value of s, denoted s_f, is unknown beforehand. Consequently, s_f must be treated as an optimization variable. To manage this, we normalize the problem by introducing a new independent variable ξ defined on the fixed interval $[0, 1]$:

$$0 = \xi_1 < \xi_2 < \cdots < \xi_N = 1 \tag{29}$$

The dynamics are then rewritten with respect to ξ [12]:

$$\frac{\mathrm{d}}{\mathrm{d}\xi}\mathbf{x}(s) = \frac{\mathrm{d}s}{\mathrm{d}\xi}\frac{\mathrm{d}}{\mathrm{d}s}\mathbf{x}(s) = \sigma\,\mathbf{x}'(s) \tag{30}$$

where the dilation factor $\sigma \coloneqq \mathrm{d}s/\mathrm{d}\xi = s_f$ is a constant for the entire trajectory. The discretized, linearized dynamics for the impulsive case at node k are:

$$\mathbf{x}_{k+1} = \begin{cases} \mathbf{A}_k\,\mathbf{x}_k + \mathbf{B}_k\,\mathbf{u}_k + \mathbf{S}_k\,\sigma + \mathbf{q}_k + \boldsymbol{\nu}_k, & \text{if } \mathbf{u}_k \neq \mathbf{0} \text{ at } \xi_k \\ \mathbf{A}_k\,\mathbf{x}_k + \mathbf{S}_k\,\sigma + \mathbf{q}_k + \boldsymbol{\nu}_k, & \text{otherwise} \end{cases} \tag{31}$$

where $(\cdot)_k \coloneqq (\cdot)(\xi_k)$ for $k = 1, \ldots, N-1$. The state transition matrices in Eqs. (10) are now formulated with respect to ξ, and the new matrix $\mathbf{S}_k$ is given by:

$$\mathbf{S}_k = \mathbf{A}_k \int_{\xi_k}^{\xi_{k+1}} \mathbf{\Phi}^{-1}(\xi, \xi_k)\,\mathbf{S}(\xi)\,\mathrm{d}\xi \tag{32}$$

This matrix is also propagated simultaneously during integration.

For low-thrust problems, the state vector is augmented with the normalized spacecraft mass ω. The dynamics in the s-domain are:

$$\mathbf{f} = \frac{\mathrm{d}}{\mathrm{d}s}\begin{bmatrix}\boldsymbol{\rho}\\ \boldsymbol{\rho}'\\ \omega\\ \tau\end{bmatrix} = \begin{bmatrix} \boldsymbol{\rho}' \\ s_0^2\,c^2\,r^{2n}\,(\mathbf{m}_1 + \mathbf{M}_2\,\boldsymbol{\rho} + m_{13}\,\nabla\Omega + \mathbf{u}) + \left(s_0\,c\,r^n\,\mathbf{M}_1 + \frac{n\,r'}{r}\,\mathbf{I}_3\right)\,\boldsymbol{\rho}' \\ -\frac{s_0\,c\,r^n}{g_0\,I_{\mathrm{sp}}}\,\Gamma \\ s_0\,c\,r^n \end{bmatrix} \tag{33}$$

While constraints from Eqs. (13c) and (13d) can be applied directly, this formulation presents a challenge: the control term $\mathbf{u}$ and its corresponding Jacobian become state-dependent due to the factor $s_0^2\,c^2\,r^{2n}$. To simplify the problem structure for SCP, we define a new control variable $\mathbf{u}^* \coloneqq s_0^2\,c^2\,r^{2n}\,\mathbf{u}$. This ensures that $\mathbf{u}^*$ appears linearly in the dynamics. The thrust magnitude is similarly transformed: $\Gamma^* \coloneqq \|\mathbf{u}^*\| = s_0^2\,c^2\,r^{2n}\,\|\mathbf{u}\|_2 = s_0^2\,c^2\,r^{2n}\,\Gamma$.

With this change of variables, the differential equation for mass becomes:

$$\frac{\mathrm{d}}{\mathrm{d}s}\omega = -\frac{1}{g_0\,I_{\mathrm{sp}}}\,\frac{1}{s_0\,c\,r^n}\,\Gamma^* \tag{34}$$

and the full system dynamics are rewritten as:

$$\mathbf{f}^* = \frac{\mathrm{d}}{\mathrm{d}s}\begin{bmatrix}\boldsymbol{\rho}\\ \boldsymbol{\rho}'\\ \omega\\ \tau\end{bmatrix} = \begin{bmatrix} \boldsymbol{\rho}' \\ s_0^2\,c^2\,r^{2n}\,(\mathbf{m}_1 + \mathbf{M}_2\,\boldsymbol{\rho} + m_{13}\,\nabla\Omega) + \left(s_0\,c\,r^n\,\mathbf{M}_1 + \frac{n\,r'}{r}\,\mathbf{I}_3\right)\,\boldsymbol{\rho}' + \mathbf{u}^* \\ -\frac{1}{g_0\,I_{\mathrm{sp}}}\,\frac{1}{s_0\,c\,r^n}\,\Gamma^* \\ s_0\,c\,r^n \end{bmatrix} \tag{35}$$

The maximum thrust constraint $\Gamma \leq T_{\max}\,\mathrm{e}^{-\omega}$ is now expressed in terms of the new variables as:

$$\Gamma^* \leq s_0^2\, c^2\, r^{2n}\, T_{\max}\,\mathrm{e}^{-\omega} \tag{36}$$

Linearizing this inequality around a reference trajectory $(\bar{r}, \bar{\boldsymbol{\rho}}, \bar{\omega})$ yields:

$$\Gamma^* \leq s_0^2\, c^2\, T_{\max}\, \bar{r}^{2n}\,\mathrm{e}^{-\bar{\omega}} \left[1 + \frac{2\,n}{r}\,(\boldsymbol{\rho} - \bar{\boldsymbol{\rho}})\,\frac{\partial r}{\partial \boldsymbol{\rho}}\Big|_{r=\bar{r}} - (\omega - \bar{\omega})\right] \tag{37}$$

The control magnitude is then constrained by $\|\mathbf{u}^*\| \leq \Gamma^*$. Our simulations show that using the dynamics in Eq. (35) with the transformed controls $\mathbf{u}^*$ and Γ^* leads to improved convergence compared to the formulation in Eq. (33).

SIMULATION AND RESULTS

To demonstrate the performance and characteristics of our proposed methods, we compute optimal trajectories in the Moon-perturbed Sun-Earth system and the rotating-pulsating frame. In particular, we investigate the convergence robustness of the Sundman-transformed SCP (Sundman-SCP) for impulsive and continuous thrust scenarios. All simulations are conducted in Python. CVXPY [13] is used to solve the convex optimization subproblems. Based on preliminary simulations, we select $n = 1$, $s_0 = 8 \times 10^3$, and $k = 15$ for the Sundman variables in the following examples.

We analyze a family of 93 transfers from a low-Earth orbit to a final state near the Moon, within the high-fidelity Sun-Earth-Moon ephemeris model. For each transfer, the initial guess is generated by propagating the initial conditions using a simpler CRTBP model, as shown in the example trajectory in Fig. 4a. More information about the guess generation can be found in [5].

This problem is challenging because of the spacecraft's proximity to Earth. This results in rapid variations in the dynamics, and these abrupt changes can degrade the accuracy of numerical integration and cause standard SCP algorithms to fail. Our tests confirm that a naive solution, such as simply increasing the number of discretization points in the physical time domain, is often insufficient to achieve convergence. In contrast, the Sundman-transformed approach, which automatically refines the discretization in these highly nonlinear regions, often converges in only a few iterations. The effect of the transformation is visible in Fig. 4b, which shows how the physical time evolves non-uniformly with respect to the new independent variable. A typical low-thrust profile is shown in Fig. 5. Due to the non-uniform time flow in the rotating-pulsating frame, the nondimensional thrust magnitude does not exhibit a constant upper bound. The scaling parameters used for nondimensionalization are themselves time-dependent, which results in a time-varying nondimensional maximum thrust constraint. This is a consideration that must be properly accounted for when formulating dynamics and constraints in such a reference frame. We compare the success rates of standard SCP and Sundman-SCP across all 93 transfers. We consider two scenarios for the initial guess: a "poor" guess, where the propagated state is far from the target, and a "good" guess, where it is relatively close. For impulsive maneuvers, the results show that Sundman-SCP achieved success rates of $48\,\%$ (poor guess) and $93\,\%$ (good guess), significantly outperforming the standard SCP's rates of $16\,\%$ and $48\,\%$, respectively.

A similar trend is observed for the continuous thrust case. For these tests, we assume an initial mass of $20\,\mathrm{kg}$, a constant maximum thrust of $5\,\mathrm{mN}$, and a specific impulse of $3000\,\mathrm{s}$. Due to the increased complexity, we only consider good initial guesses. Sundman-SCP successfully converged

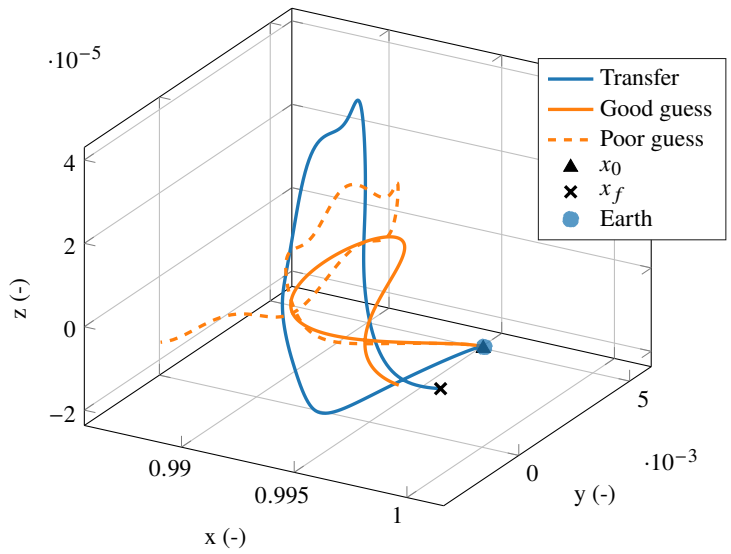

(a) Transfer orbit and initial guess.

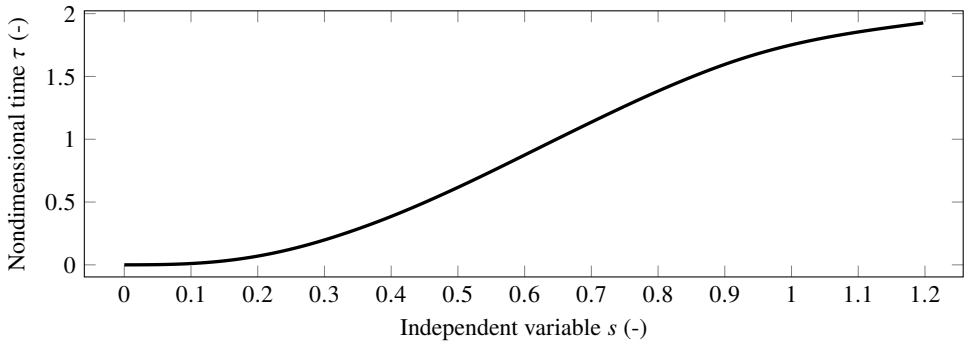

(b) Evolution of nondimensional time.

Figure 4: Transfer orbit and evolution of nondimensional time.

in 70 % of cases, compared to just 48 % for the standard SCP. These results show that the Sundman transformation can enhance the convergence and robustness of SCP for complex multi-body trajectory optimization problems.

CONCLUSION

This paper introduces a Sundman transformation to improve convergence of SCP for trajectory design in high-fidelity multi-body models in the rotating-pulsating frame. By placing more discretization nodes near the primaries where the transformed dynamics evolve more slowly, the method enables convergence even when trajectories pass close to these bodies. Our extension to continuous-thrust problems shows the potential of the approach for more general mission scenarios. Our preliminary results indicate an improved convergence behavior for both impulsive and low-thrust transfers.

While the transformation introduces more complexity in the dynamics and requires additional user-selected parameters, it provides a straightforward way to automatically increase node density

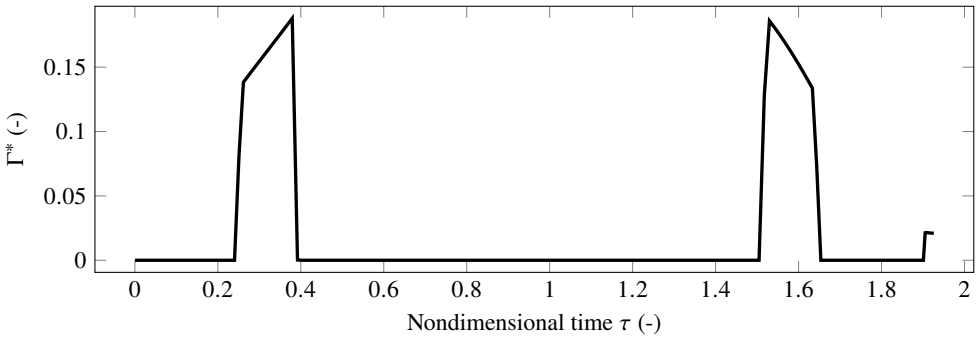

(a) Nondimensional thrust magnitude Γ^*.

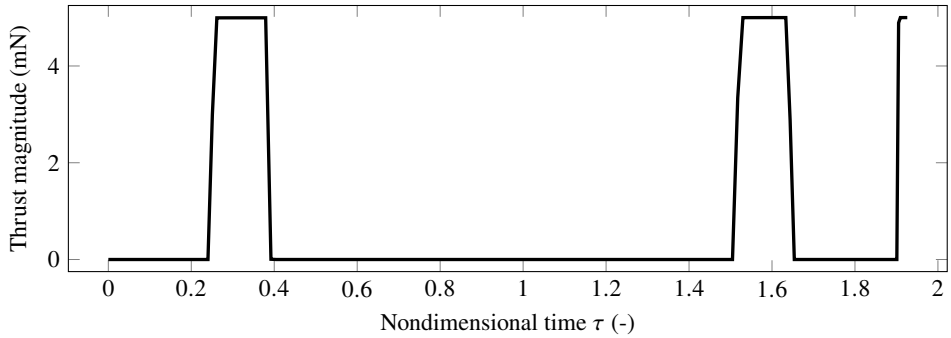

(b) Dimensional thrust magnitude.

Figure 5: Nondimensional and dimensional thrust magnitude obtained with low thrust in the ephemeris model and rotating-pulsating frame.

where it is most needed. At the same time, optimizing in the transformed domain can enhance the convergence behavior, especially in regions where traditional SCP methods often struggle.

ACKNOWLEDGMENTS

From the MIT side, this work was funded under the Air Force Office of Scientific Research (AFOSR) Space University Research Initiative grant (FA95502210092).

At Politecnico di Milano, Ethan R. Burnett was funded by the European Union (Horizon Europe, FAAST-MSCA, Grant ID: 101063274). Views and opinions expressed are however those of the authors only and do not necessarily reflect those of the European Union, the European Research Executive Agency, or the European Research Council. Neither the European Union nor the granting authority can be held responsible for them.

APPENDIX: DERIVATIVES

The elements of the Jacobian matrix in Eq. (26) are:

$$\frac{\partial \boldsymbol{\rho}'}{\partial \boldsymbol{\rho}} = \mathbf{0}_3 \tag{38a}$$

$$\frac{\partial \boldsymbol{\rho}'}{\partial \boldsymbol{\rho}'} = \mathbf{I}_3 \tag{38b}$$

$$\frac{\partial \boldsymbol{\rho}'}{\partial \tau} = [0,0,0]^\top \tag{38c}$$

$$\begin{aligned}\frac{\partial \boldsymbol{\rho}''}{\partial \boldsymbol{\rho}} = {} & s_0^2\, c^2 \left[2\, n\, r^{2n-1} \left(\mathbf{m}_1 + \mathbf{M}_3\, \boldsymbol{\rho} + m_{13}\, [\nabla\Omega]^\top\right) \frac{\partial r}{\partial \boldsymbol{\rho}} + r^{2n}\, \mathbf{M}_3 + r^{2n}\, m_{13}\, \frac{\partial \nabla\Omega}{\partial \boldsymbol{\rho}}\right] \\ & + s_0\, c\, n\, r^{n-1}\, \mathbf{M}_2\, \boldsymbol{\rho}'\, \frac{\partial r}{\partial \boldsymbol{\rho}} - \frac{n\, r'}{r^2}\, \boldsymbol{\rho}'\, \frac{\partial r}{\partial \boldsymbol{\rho}} + \frac{n}{r}\, \boldsymbol{\rho}'\, \frac{\partial r'}{\partial \boldsymbol{\rho}}\end{aligned} \tag{38d}$$

$$\frac{\partial \boldsymbol{\rho}''}{\partial \boldsymbol{\rho}'} = s_0\, c\, r^n\, \mathbf{M}_2 + \frac{n\, r'}{r}\, \mathbf{I}_3 + \frac{n}{r}\, \boldsymbol{\rho}'\, \frac{\partial r'}{\partial \boldsymbol{\rho}'} \tag{38e}$$

$$\frac{\partial \tau'}{\partial \boldsymbol{\rho}} = s_0\, c\, n\, r^{n-1}\, \frac{\partial r}{\partial \boldsymbol{\rho}} \tag{38f}$$

$$\frac{\partial \tau'}{\partial \boldsymbol{\rho}'} = [0,0,0] \tag{38g}$$

$$\frac{\partial \tau'}{\partial \tau} = 0 \tag{38h}$$

where $\mathbf{0}_3$ is the 3×3 zero matrix, and

$$\frac{\partial \nabla\Omega}{\partial \boldsymbol{\rho}} = \sum_{j \in \mathcal{S}} \mu_j \left[-\frac{\mathbf{I}_3}{\|\boldsymbol{\rho} - \boldsymbol{\rho}_j\|^3} + \frac{3\,(\boldsymbol{\rho} - \boldsymbol{\rho}_j)\,(\boldsymbol{\rho} - \boldsymbol{\rho}_j)^\top}{\|\boldsymbol{\rho} - \boldsymbol{\rho}_j\|^5}\right] \tag{39}$$

The set $\mathcal{S}$ refers to the two primaries and other perturbing bodies. We consider three cases for the definition of r: r is the distance to the first primary r_p, to the second primary r_s, or a weighted distance.

For the distance to the first and second primary, we have $\mathbf{r} \coloneqq \boldsymbol{\rho} + \mu\, \mathbf{i}_x$ and $\mathbf{r} \coloneqq \boldsymbol{\rho} + (\mu - 1)\, \mathbf{i}_x$, respectively. The derivatives are then

$$\frac{\partial r}{\partial \boldsymbol{\rho}} = \frac{1}{r}\, \mathbf{r}^\top \tag{40}$$

$$\frac{\partial r'}{\partial \boldsymbol{\rho}} = -\frac{1}{r^2}\, \mathbf{r}^\top \boldsymbol{\rho}'\, \frac{\partial r}{\partial \boldsymbol{\rho}} + \frac{1}{r}\, [\boldsymbol{\rho}']^\top \tag{41}$$

$$\frac{\partial r'}{\partial \boldsymbol{\rho}'} = \frac{1}{r}\, \mathbf{r}^\top \tag{42}$$

If a weighted distance is used for r, we can define

$$r \coloneqq A^{\frac{1}{n}} \tag{43}$$

where $A \coloneqq w\, r_p^n + (1 - w)\, r_s^n$. Therefore,

$$\frac{\partial r}{\partial \boldsymbol{\rho}} = \frac{1}{n}\, A^{\frac{1}{n} - 1}\, \frac{\partial A}{\partial \boldsymbol{\rho}} \tag{44}$$

and

$$\frac{\partial A}{\partial \boldsymbol{\rho}} = \left(r_p^n - r_s^n\right) \frac{\partial w}{\partial \boldsymbol{\rho}} + w\, n\, r_p^{n-1} \frac{\partial r_p}{\partial \boldsymbol{\rho}} + (1-w)\, n\, r_s^{n-1} \frac{\partial r_s}{\partial \boldsymbol{\rho}} \tag{45}$$

Moreover,

$$\frac{\partial w}{\partial \boldsymbol{\rho}} = -w^2\, k \left(\frac{r_p}{r_s}\right)^k \left(\frac{1}{r_p} \frac{\partial r_p}{\partial \boldsymbol{\rho}} - \frac{1}{r_s} \frac{\partial r_s}{\partial \boldsymbol{\rho}}\right) \tag{46}$$

where $\partial r_p / \partial \boldsymbol{\rho}$ and $\partial r_s / \partial \boldsymbol{\rho}$ are given by Eq. (40). The expression for $\partial r' / \partial \boldsymbol{\rho}$ reads

$$\frac{\partial r'}{\partial \boldsymbol{\rho}} = \frac{1}{n^2} A^{\frac{1}{n}-2} \left((1-n) \frac{\partial A}{\partial \boldsymbol{\rho}} \left(\frac{\partial A}{\partial \boldsymbol{\rho}} \boldsymbol{\rho}'\right) + n\, A\, [\rho']^\top \frac{\partial^2 A}{\partial \boldsymbol{\rho}\, \partial \boldsymbol{\rho}^\top}\right) \tag{47}$$

As the expression for the second derivative $\partial^2 A / (\partial \boldsymbol{\rho}\, \partial \boldsymbol{\rho}^\top)$ is quite lengthy, it is omitted here for the sake of conciseness.

REFERENCES

[1] D. C. Folta and K. C. Howell, "Evolution of Astrodynamics for Multibody Environments, Numerical Precision and Dynamical Understanding," *AAS/AIAA Astrodynamics Specialist Conference*, 2023. Paper AAS 23-244.

[2] W. S. Koon, M. W. Lo, J. E. Marsden, and S. D. Ross, "Dynamical Systems, The Three-Body Problem and Space Mission Design," California Institute of Technology, 2006.

[3] B. Park, R. R. Sanaga, and K. Howell, "Numerical Assessment of Intermediate Models in a Frequency-Based Hierarchy for the Cislunar Domain," *AAS/AIAA Space Flight Mechanics Meeting*, 1 2025. Paper AAS 25-161.

[4] R. R. Sanaga, B. Park, and K. C. Howell, "A Unified Numerical Transition Scheme Between Dynamical Models within Cislunar Space," *AAS/AIAA Space Flight Mechanics Meeting*, 1 2025. Paper AAS 25-238.

[5] K. Xi, H. Chunton, C. Hofmann, G. Lavezzi, E. R. Burnett, F. Topputo, and R. Linares, "A Homotopic Convex Optimization Approach for Trajectory Design in Multi-Body Models," *AAS/AIAA Space Flight Mechanics Meeting*, 1 2025. Paper AAS 25-385.

[6] B. Park and K. C. Howell, "Assessment of dynamical models for transitioning from the Circular Restricted Three-Body Problem to an ephemeris model with applications," *Celestial Mechanics and Dynamical Astronomy*, Vol. 136, No. 1, 2024, 10.1007/s10569-023-10178-9.

[7] E. Veruari, "Space Trajectory Optimisation in High Fidelity Models," Master Thesis, Politecnico di Milano, 2016.

[8] Y. Mao, M. Szmuk, X. Xu, and B. Açıkmeşe, "Successive Convexification: A Superlinearly Convergent Algorithm for Non-convex Optimal Control Problems," `https://arxiv.org/abs/1804.06539`, Preprint, submitted February 2019.

[9] M. Berry and L. Healy, "The generalized Sundman transformation for propagation of high-eccentricity elliptical orbits," *Proceedings of the 12th AAS/AIAA Space Flight Mechanics Meeting*, Vol. 112, 01 2002.

[10] J. D. Aziz, J. S. Parker, D. J. Scheeres, and J. A. Englander, "Low-Thrust Many-Revolution Trajectory Optimization via Differential Dynamic Programming and a Sundman Transformation," *The Journal of the Astronautical Sciences*, Vol. 65, No. 2, 2018, pp. 205–228.

[11] C. H. Yam, D. D. Lorenzo, and D. Izzo, "Towards a high fidelity direct transcription method for optimisation of low-thrust trajectories," *International Conference on Astrodynamics Tools and Techniques (ICATT)*, 2010.

[12] M. Szmuk, T. P. Reynolds, and B. Açıkmeşe, "Successive Convexification for Real-Time Six-Degree-of-Freedom Powered Descent Guidance with State-Triggered Constraints," *Journal of Guidance, Control, and Dynamics*, Vol. 43, No. 8, 2020, pp. 1399–1413, 10.2514/1.G004549.

[13] S. Diamond and S. Boyd, "CVXPY: A Python-Embedded Modeling Language for Convex Optimization," *Journal of Machine Learning Research*, 2016. To appear.